Reassessment of Large Dipole Moment Enhancements in Crystals: A Detailed Experimental and Theoretical Charge Density Analysis of 2-Methyl-4-nitroaniline

Andrew E. Whitten[†]

Chemistry, University of New England, Armidale NSW 2351, Australia

Peter Turner

School of Chemistry, University of Sydney, Sydney NSW 2000, Australia

Wim T. Klooster and Ross O. Piltz

Bragg Institute, Australian Nuclear Science and Technology Organization, PMB 1, Menai NSW 2234, Australia

Mark A. Spackman*

Chemistry − M313, University of Western Australia, Crawley WA 6009, Australia

Received: March 23, 2006; In Final Form: May 17, 2006

The molecular dipole moment of MNA in the crystal has been critically reexamined, to test the conclusion from an earlier experimental charge density analysis that it was substantially enhanced due to a combination of strong intermolecular interactions and crystal field effects. X-ray and neutron diffraction data have been carefully measured at 100 K and supplemented with ab initio crystal Hartree−Fock calculations. Considerable care taken in the measurement and reduction of the experimental data excluded most systematic errors, and sources of error and their effects on the experimental electron density have been carefully investigated. The electron density derived from a fit to theoretical structure factors assisted in the determination of the scale and thermal motion model. The dipole moment enhancement for MNA in the crystal is much less than that reported previously and only on the order of 30−40% (∼2.5 D). In addition to the dipole moment, experimental deformation electron density maps, bond critical point data, electric field gradients at hydrogen nuclei, and atomic and group charges all agree well with theoretical results and trends. Anisotropic modeling of the motion of hydrogen atoms, integral use of periodic ab initio calculations, and improved data quality are all aspects of this study that represent a considerable advance over previous work.

Introduction

Development of visible light lasers via frequency doubling, electrooptical devices for optical signal processing, high-speed optical communications, and compact data storage all involve exploitation of nonlinear optical (NLO) properties of appropriate materials. Organic molecular crystals are attractive candidates for such materials, as well-established methods of synthetic chemistry enable almost continuous modification of NLO properties. Certain classes of organic materials, especially those with highly delocalized π electrons and additional donor/acceptor groups at opposite ends of the molecule, exhibit extremely large NLO effects, and many organic NLO crystals exhibit high optical damage thresholds, making them attractive in high-power applications.[1−4] Properties of 2-methyl-4-nitroaniline (MNA), especially in the solid state, have been the focus of a large number of investigations since the late 1970s, when it was discovered that crystals of this compound exhibited an exceptionally large second-order optical nonlinearity and linear electrooptic effect,[5−7] and interest in MNA and related molecules has remained strong because their unique properties promise potentially important applications.

The optical and related properties of MNA were investigated with some enthusiasm in the late 1980s and early 1990s, including determination of electrooptical coefficients[8,9] and refractive indices,[10] observation of phase-matched second harmonic generation in optical waveguides,[11] measurement of the piezoelectric tensor,[12,13] and molecular reorientation in the crystal induced by an external electric field.[14] At the same time, the electrostatic properties of the molecule in the crystal were investigated by Howard and co-workers in a careful combined experimental and theoretical charge density study.[15] The controversial results of that study showed that the dipole moment of the molecule was enhanced upon crystallization by a factor of almost 3, to 23 D, due apparently to crystal field effects inducing substantial polarization of the electron distribution. This apparent enhancement was accompanied by an estimated standard deviation (esd) of 8 D, meaning it is possible that within two standard deviations the dipole moment is unaltered or is increased to almost 40 D. Although the study reported a high level of model dependency in relation to the magnitude of polarization for the molecule, the experimental findings were backed by theoretical evidence that an applied field approximat-

* To whom correspondence should be addressed. Email: mas@cyllene.uwa.edu.au. Fax: +61 8 6488 1005.

[†] Present address: Bragg Institute, Australian Nuclear Science and Technology Organization, PMB 1, Menai NSW 2234, Australia.

10.1021/jp061830n CCC: $33.50
Published on Web 06/16/2006

ing in a crystalline environment induced a dipole moment in agreement with the experimental value.

Largely due to the findings reported by Howard et al.,[15] MNA has been recognized widely as an important example of a compound that exhibits considerable dipole moment enhancement in the solid state. In particular, that work has been cited in studies regarding the properties of molecules crystallizing in acentric space groups,[16−18] in charge density studies where dipole moment enhancement is observed[19−22] (in particular, apparent enhancements greater than 100%[23−26]), and research concerning the effect of the crystal field on a molecule.[27−32] It is well-established, both experimentally and theoretically, that molecules undergo charge redistribution upon crystallization, generally causing an enhancement of the molecular dipole moment (although this is not necessarily the case) and the magnitude is typically on the order of 30% for hydrogen-bonded systems. Although electrostatic moments have been extracted from X-ray diffraction data almost routinely for some time,[33,34] there is increasing recognition that the results can be highly dependent on the multipole model fitted to the X-ray structure factors.[35] It is also noteworthy that almost all the experimental studies that have reported dipole moment enhancements greater than 100%[15,23−26,36] were for materials crystallizing in noncentrosymmetric space groups, and the charge density studies treated the thermal motion of hydrogen atoms as isotropic. Exceptions worthy of note are enhancements of ∼300% reported for two polymorphs of *p*-nitrophenol in centrosymmetric space groups $P2_1/c$ and $P2_1/n$[24] and an enhancement of ∼150% for 1-(2-hydroxy-5-nitrophenyl)ethanone which, although in the noncentrosymmetric space group $Pca2_1$, incorporated neutron diffraction estimates of hydrogen atom anisotropic displacement parameters (ADPs) in the charge density analysis.[37]

These considerations led us to question whether the large dipole moment enhancements reported to date are real, and even whether they can be reliably determined experimentally. We refer the reader to a comprehensive summary of recent charge density studies reporting molecular dipole moments, where these issues are critically investigated.[38] However, the study on MNA has clearly set a precedent for the acceptance of such large enhancements of the dipole moment, and for this reason, it was worthy of detailed reinvestigation, to either confirm or to dismiss the previous findings. In addition, it is structurally one of the simplest compounds where such significant enhancements have been observed, and with the advent of routine low-temperature data collection and CCD technology, the task of measuring a highly redundant, high-resolution data set is now much less formidable than in the past.

The present study utilizes neutron diffraction data and crystal Hartree−Fock calculations to complement the multipole modeling of X-ray diffraction data. All issues faced in the treatment of experimental data are discussed in detail, as well as the measures taken to counter them. In addition to the molecular dipole moment, we report a variety of properties including atomic charges, properties derived from a topological analysis of the electron density, and electric field gradients at hydrogen nuclei, all of which are compared with independent experimental measurements where available and with theoretical calculations.

Experimental Section and Calculation Method

X-ray Diffraction Data Collection and Reduction. Preliminary crystallization of MNA (Fluka, 98% purity) yielded orange crystals, contrary to the report by Howard et al.[15] but in agreement with a recent study by Ferguson et al.[39] As it was likely that the orange color was due to impurities, MNA powder was purified by decolorization with activated charcoal, resulting in pale yellow crystals. The purified product was added to a 1:1 solution of toluene and methanol at 30 °C, until the mixture was almost saturated, and the flask was left open to the atmosphere until crystals began to form, at which time it was stoppered and the temperature slowly lowered by approximately 0.5 °C per day. After a week, the solution contained numerous crystals that were relatively long and flat, with approximate dimensions of 0.2 × 0.3 × 5.0 mm^3. The crystals were very soft and easily damaged but cleaved well approximately perpendicular to the long growth axis.

X-ray diffraction data were measured at the University of Sydney using a Bruker SMART 1000 CCD diffractometer. A graphite-monochromated Mo Kα X-ray beam was produced from a sealed tube with a current of 40 mA and a voltage of 50 kV. A cleaved fragment of an MNA crystal was attached with Exxon Paratone N to a short length of fiber supported on a thin piece of wire inserted in a steel mounting pin. The crystal was cooled to 100(2) K with an Oxford Cryosystems Cryostream and maintained at this temperature for the duration of the experiment. Data collection was undertaken in three spheres with the camera at 30°, 65°, and 100° in 2θ and 39.61 mm from the crystal. Each sphere was collected using ω scan increments of 0.2° and with the ϕ axis at 0°, 90°, 180°, and 270° for the first two spheres, and 0°, 120° and 240° for the last sphere. Exposure times were 20, 35, and 60 s, respectively, for each of the three camera positions. In addition, the first 50 frames of each sphere were recollected at the completion of the sphere to assess decay.

The data were integrated with SAINT[40] using the BLEND option, and box sizes were chosen such that the maximum profile on the boundary in the *x*, *y*, and *z* dimensions was less than 10%, which corresponded to values of $x = 1.2$, $y = 1.5$, and $z = 1.1$. These optimum parameters were determined for the high-angle data (camera positioned at $2\theta = 100°$) and then used to integrate all data. The data were scaled and merged using SORTAV[41] according to the Laue symmetry, as anomalous dispersion was decided not to be a significant effect. Many different aspects of the data reduction were investigated, in particular, the box sizes used in the integration. Although the determination of box sizes and the dispersion of the Mo Kα beam are interconnected, and have been examined by Lenstra, Rousseau, and co-workers,[42,43] tests carried out on the MNA data exclude the possibility that dispersion of the Mo Kα beam is compromising the results. This was tested by reintegration of the data with much larger box sizes ($x = y = z = 3.0$). While the refined thermal parameters were slightly different between refinements using data integrated with different box sizes, no significant differences were found between the electronic parameters of multipole refinements.

During initial data refinements, large differences of approximately 30 e between $|F_o|$ and $|F_c|$ were observed for the $(\bar{1}12)$ reflection. When the raw frames were examined, it was apparent that the response of the detector had become nonlinear or an overflow had occurred, and as a consequence, the reflection profile was truncated; symmetry-equivalent reflections also displayed the same behavior. As this very intense reflection at low angle ($\sin\theta/\lambda = 0.15$ $Å^{-1}$) was considered important, the SMART data were supplemented with low-angle data measured previously using a synchrotron source at ESRF at the same wavelength.[44] During that experiment, one set of frames was measured using a 150 μm Cu filter, which allowed the intense portion of the low-angle data to be measured without truncation. Reflections measured more than once, and for which

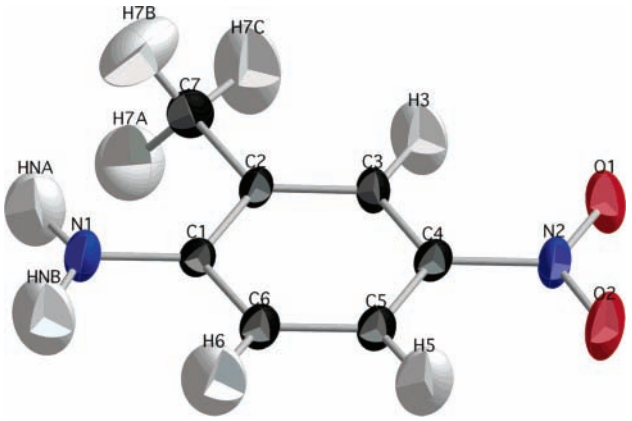

Figure 1. ORTEP plot for MNA based on refinement of neutron diffraction data (99% probability level).

agreement was within 2.5% of the mean for that group, were included in the scaling and merging of the SMART data, resulting in a much better estimate of the magnitude of the $(\bar{1}12)$ reflection.

Neutron Diffraction Data Collection and Reduction. The crystal used in the neutron diffraction experiment was grown by a modified Bridgman technique.[45] The pale yellow crystal was roughly the shape of a truncated cone 5 mm in length, with diameters of approximately 6 mm and 4 mm at each of the ends, and was wrapped in greased aluminum foil and glued to an aluminum pin mounted on the Huber four-circle diffractometer (2TANA) at the HIFAR reactor located at Lucas Heights, Australia. The temperature was lowered to 100(2) K using a Displex closed-cycle helium refrigerator, and data was collected on a full set of reflections to 110° in 2θ , using $\omega-2\theta$ scans. Data reduction was carried out with in-house ANSTO programs, including an analytic absorption correction and corrections for multiple scattering.

Initial Refinements. Initial refinements with the neutron data were performed using VALRAY,[46] starting with the atomic coordinates reported by Howard et al.,[15] translated so that the coordinates of O(2) were (1.0, y < 0.5, 0.5). The x and z coordinates of this atom were then fixed to define the origin of the polar space group, while all other position and anisotropic displacement parameters were refined for the neutron data. An ORTEP representation of the resulting structure is shown in Figure 1. Similar refinements were also carried out for the X-ray data using spherical atom scattering factors and with hydrogen position and thermal parameters fixed at the neutron values. Crystal, experimental, and refinement details are summarized in Table 1.

Theoretical Calculations. A limitation of the previous charge density study on MNA was the lack of available computing power, which meant that periodic calculations on relatively large systems such as MNA were out of reach, even with inexpensive basis sets such as the split valence 6-31G. To compensate for this, Howard et al.[15] simulated crystal field effects with calculations on an isolated molecule in the presence of an applied electric field of magnitude determined with the "Lorentz factor tensor" formalism,[47] using the molecular dipole from the zero-field calculation to estimate the electric field at a lattice point. The molecular dipole moment resulting from this calculation supported the claim of a large enhancement of the dipole in the crystal, but as acknowledged by those authors, this applied field represents only a zeroth-order approximation to the crystal field. The actual field experienced by a molecule in the crystal is highly anisotropic, and consequently, a uniform field is unlikely to model the crystal field effectively. Periodic ab initio calculations, on the other hand, should give a reliable estimate of the polarization of the electron density and indicate whether the previous results from the finite field calculation are realistic.

Theoretical calculations for crystalline MNA were performed using the structural parameters derived from the neutron diffraction data. All results reported below are based on periodic Hartree−Fock calculations with *CRYSTAL98*,[48] using the DZP basis set[49] and thresholds for numerical accuracy and convergence described previously.[50,51] The ab initio calculations were repeated using the MOLSPLIT option in *CRYSTAL98* to obtain an electron distribution due to a superposition of noninteracting molecules (referred to below as "molecules").

Determination of Multipole Model by Fitting to Theoretical Structure Factors. The fitting of theoretical structure factors to complement experimental charge density studies is now quite common,[52−54] and in difficult cases, it can aid in the determination of radial parameters. It avoids many of the problems associated with experimental data: there are no experimental errors or thermal motion, the scale is known, no extinction correction is required, and the phases of all structure factors are known. The last point may seem of minor importance, as phases are also unknown from the diffraction experiment. However, because they are known from a theoretical calculation, their incorporation into the fitting process removes errors in the model due to phase ambiguity in noncentrosymmetric space groups.[18] Recently, VALRAY has been modified to refine multipole models against both the real and imaginary components of the structure factor for the purpose of a combined X-ray and convergent beam electron diffraction (CBED) study,[55] where both the magnitude and the phase of several low-angle structure factors were obtained from the CBED experiment and incorporated into the multipole refinement of X-ray data. This capability presents an opportunity in the fitting of theoretical data for MNA, avoiding the introduction of ambiguity in the model populations and radial parameters, which is known to be an issue for this compound.[15]

There are also practical reasons for fitting theoretical structure factors in this case. Preliminary multipole refinements identified problems associated with the determination of the scale of the X-ray data and also possible anharmonic thermal motion of the oxygen atoms. The populations from multipole refinement against theoretical structure factors can be imposed on the experimental data in order to refine anharmonic thermal parameters without joint refinement of both electronic and thermal parameters at the same time, which usually results in large correlations. This also allows the scale of the X-ray data to be determined more reliably.

A set of structure factors at the same resolution as the experiment, $(\sin\theta/\lambda)_{max} = 1.27$ Å^{-1}, was generated using the electron density from the *CRYSTAL98* Hartree−Fock calculation. Each structure factor was multiplied by a factor of $\exp[-2.0(\sin\theta/\lambda)^2]$, to mimic the effects of thermal motion. It has been shown previously that electrostatic properties are reproduced more reliably when this weighting factor is introduced,[18,56] as it effectively downweights the high-angle data, which can otherwise dominate the least-squares refinement. The generalized X-ray scattering-factor model implemented in VALRAY was used for multipole modeling of theoretical structure factors, minimizing the residual

$$\Delta = \sum_{\mathbf{h}} \{[A_{C98}(\mathbf{h}) - A_{mult}(\mathbf{h})]^2 + [B_{C98}(\mathbf{h}) - B_{mult}(\mathbf{h})]^2\} \quad (1)$$

where $A(\mathbf{h})$ and $B(\mathbf{h})$ are the real and imaginary components of

TABLE 1: Summary of the Crystal, Experimental, and Refinement Details for MNA

	X-ray	neutron
	crystal data	
chemical formula	$C_7H_8N_2O_2$	
chemical formula weight	152.14	
cell setting	monoclinic, *Ia*	
a, *b*, *c* (Å)	8.1669(4), 11.5636(6), 7.4128(4)	8.131(2), 11.515(2), 7.371(2)
β (°)	93.312(3)	93.19(2)
V (Å^3)	698.89(8)	689.1(4)
F(000)	320	187.7
Z	4	4
D_c (g cm^{-3})	1.45	1.47
crystal form	platelet with beveled edges	truncated cone
crystal size (mm^3)	0.12 × 0.20 × 0.55	5.0 × 5.0 × 7.0
crystal color	yellow	yellow
	data collection	
radiation type	Mo Kα	neutron, reactor source
wavelength (Å)	0.71073	1.235
# reflections for cell	987 ($10° \le 2\theta \le 128°$)	46 ($10° \le 2\theta \le 74°$)
μ (mm^{-1})	0.1086	0.20
temperature (K)	100(2)	100(2)
diffractometer	Bruker SMART 1000 CCD	Huber 4-circle, BF_3 detector
no. of measured reflections	26425	1482
no. of unique data	5683	848
completeness (Laue)	95.0%	98.8%
redundancy (average)	4.6	1.7
R_{int}	0.0247	0.0125
$(\sin\theta/\lambda)_{max}$ (Å^{-1})	1.27	0.66
range of *h*, *k*, *l*	$-20 \le h \le 20$, $-28 \le k \le 28$, $-18 \le l \le 17$	$-10 \le h \le 10$, $0 \le k \le 15$, $-7 \le l \le 9$
	conventional refinement details	
refinement on	$F > 4\sigma(F)$	$F > 9\sigma(F)$
N_{obs}, N_{par}	5055, 99	847, 171
$R(F)$, $R_w(F)$, GoF	0.0309, 0.0374, 3.38	0.0206, 0.0218, 3.48
weighting scheme	$\sigma^{-2}(F)$	$\sigma^{-2}(F)$
$g \times 10^{-4}$ radians^{-1}	0.014(6)	0.118(4)
$y_{ext,min}(F)$	0.984	0.792
source of atomic scattering factors	calculated in VALRAY using atomic wave functions[58]	International Tables for Crystallography: Vol. C[73]
	multipole refinement details	
N_{obs}, N_{par}	5055, 383	
$R(F)$, $R_w(F)$, GoF	0.0156, 0.0171, 1.44	
weighting scheme	$\sigma^{-2}(F)$	
$g \times 10^{-4}$ radians^{-1}	0.0759(4)	
$y_{ext,min}(F)$	0.919	

the structure factor, respectively, and the expression implies use of unit weights. For heavy atoms, multipoles up to the octopole level were used, with the radial functions for the monopoles, dipoles, and quadrupoles constructed from products of localized atomic orbitals[57] based on the Clementi−Roetti atomic wave functions.[58] The radial functions used for the octopoles were single exponential, $r^n \exp(-\alpha r)$, with $n = 3$. The radial functions for hydrogen atom monopoles, dipoles, and quadrupoles were all single exponentials as described above, with $n = 0$, 1, and 2 for monopole, dipoles, and quadrupoles, respectively. Since the scale of the theoretical data was known exactly, F(000) was included in the refinement to ensure the correct scale. All multipole populations were refined, as were the radial scaling parameters κ_0, κ_1, κ_2, and α_3 for C, N, and O, and α_0, α_1, and α_2 for hydrogen atoms. Core populations of C, N, and O were constrained to be equal, as were κ_0, κ_1, and κ_2 for each atom and all radial scaling parameters for all hydrogen atoms. In addition, all exponents for the octopole radial functions were constrained to be equal for ring C and for both oxygen atoms, with the methyl carbon, the nitro, and the amino nitrogen refined unconstrained. No symmetry constraints were imposed on any multipole populations.

Problems Determining the Scale of the X-ray Data. While the impact of the scale factor on the results of a multipole refinement is rarely discussed in any depth, its importance was recognized very early,[59] and corrections for effects such as anomalous dispersion and extinction rely on the absolute scale of the data being known. Scaling of the experimental data in VALRAY is performed without explicitly refining a scale factor; instead, the monopole populations are used to scale the data, and estimates of Fourier and direct space properties and all populations (or structure factors) are scaled by $k = F(000)/\sum_i(P_i^{core} + P_i^{valence})$. Whether the scale is determined in this manner or as a parameter in the least-squares refinement, it will depend largely on the high-angle data, as the density of observations increases with $(\sin\theta/\lambda)^3$. For MNA, over half the present data are beyond 0.95 Å^{-1}, so systematic errors in the high-angle data will cause the scale to be incorrectly determined and impact on the valence features of the model electron density. The present study reveals that the estimated charge redistribution in the molecule correlates with the scale, and the scale implied when the least-squares residual is at a minimum yields results that have little physical basis.

For MNA, part of the problem is due to the almost total variability in the phases of the data. Noncentrosymmetric crystal structures are well-known to present a challenge for charge density analysis; one of the worst cases observed for molecular crystals is hexamethylenetetramine (space group $I\bar{4}3m$), for which multiple least-squares solutions were obtained.[60] How-

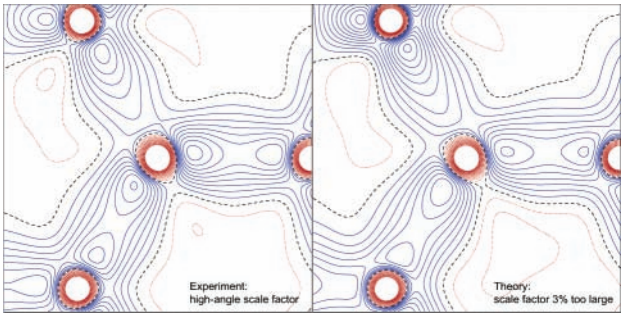

Figure 2. Static model deformation density maps, $\rho_{calc}(\mathbf{r}) - \rho_{IAM}(\mathbf{r})$ for MNA showing features in the bonds involving C(4). Solid contours (blue) indicate positive regions; dotted contours (red) indicate negative regions, with zero contours represented by dashed lines (black). The contour interval is 0.1 e Å^{-3}. Left: X-ray, using a scale factor determined from a high-angle refinement. Right: theoretical, after an incorrect scale factor has been imposed and isotropic thermal parameters have been refined.

ever, not all noncentrosymmetric space groups exhibit ambiguity in phases to the same extent, because some point group symmetries dictate the phases of some reflections. For example, for urea, some 33% of reflections have restricted phases (for a dataset with sin $\theta/\lambda < 1.0$ Å $^{-1}$), while for MNA, a maximum of 15 of 6432 reflections, or only 0.23%, are restricted by symmetry (for a dataset with the same resolution as the present X-ray data).

The usual practice when modeling X-ray data from acentric compounds is to fix thermal parameters and scale at values determined by a high-angle refinement, to avoid correlations between thermal motion and electronic parameters. Since VALRAY does not refine a scale factor, instead using the monopole populations to scale the data, the scale cannot be fixed in this manner, and it is possible that the thermal parameters deduced from a high-angle refinement have been determined on a different scale from that of the electronic parameters. To enforce a certain scale, a restraint can be included in the refinement, whereby $F(000)$ is included as a data point, and the degree to which this restraint is enforced is governed by the value assumed for $\sigma[F(000)]$.

During multipole modeling of the MNA data, refinement of thermal and positional parameters in a high-angle refinement yielded a scale factor that is 6% higher than that obtained from subsequent refinement of the electronic parameters (while leaving the thermal and positional parameters fixed at the values inferred from the high-angle refinement). The resulting refinement statistics are acceptable, but Figure 2 (left image) shows that unphysical artifacts appear in the deformation density maps in the form of peaks close to the atoms, instead of the center of the bond. To investigate the effect of imposition of the incorrect scale upon the model density, a refinement was performed against the theoretical structure factor magnitudes (i.e., unphased), refining isotropic thermal parameters, with an imposed scale on the data that was 3% too large on $|F|$; these thermal parameters were subsequently fixed, and multipole population and radial parameters were then refined. The result, shown in Figure 2 (right image), provides strong evidence that the overall scale factor obtained from multipole modeling of the X-ray data was not consistent with the low-angle data, as the features in both maps—one obtained from theory, the other from experiment—are almost identical. In addition, we observed that the molecular dipole moment estimated from this refinement increases from ~12 D to ~27 D, simply by refining thermal parameters at a scale that is overestimated, then proceeding with the refinement of population and other parameters.

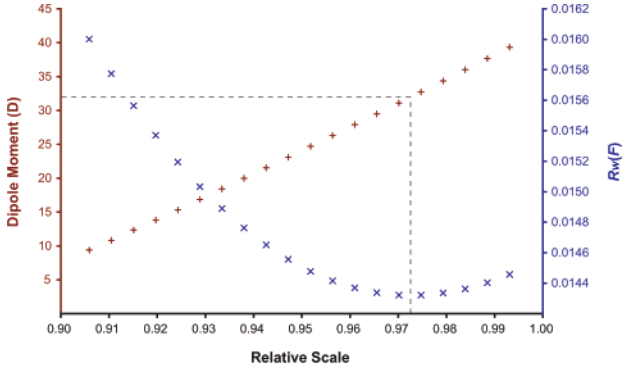

Figure 3. The dependence of the molecular dipole moment and $R_w(F)$ on assumed scale of the X-ray data.

To investigate this phenomenon further, tests were carried out with the experimental data to determine the dependence of the dipole moment and the refinement statistics on the assumed scale of the data. A refinement as described above was performed against the X-ray data, except in the first cycles, positional and thermal parameters were varied, followed by a multipole refinement, keeping the thermal and positional parameters fixed, all at a variety of different scale factors enforced by a restraint. The results (Figure 3) show that the dipole moment of the molecule is strongly, and almost linearly, dependent on the assumed scale, and the dipole moment implied by the minimum in the least-squares residual $R_w(F)$ is over 30 D (see dashed lines in Figure 3).

It appears that in some circumstances data integrated with the program SAINT displays scale differences between the high- and low-angle data.[61] This problem can be countered to some extent by dividing the data into high- and low-angle batches and employing different scale factors for each.[62] This is equivalent to the method used in recent charge density analyses by Stalke and co-workers, where data is collected with two nonoverlapping camera positions, and the scale for each batch is refined separately during the multipole refinement.[63,64] If the present high-angle data are on a different scale and are dominating the contribution to the determination of the scale factor, then it follows that refinement with a lower resolution cutoff should lead to a different scale factor. This was indeed found to be the case when the procedure described above was performed using a resolution limit on the data of 1.1 Å^{-1}: the minimum with respect to $R_w(F)$ now occurs at relative scale near 0.957 and for a dipole moment of ~28 D. These results demonstrate that the dipole moment is more-or-less arbitrary, unless the scale can be accurately determined, and if the scale of the data is not defined by a minimum in the residual with respect to the refined parameters, as with the present data, then it must be estimated in a different manner. In the absence of any other experimental evidence, we decided to use the theoretical structure factors to aid in the determination of the experimental scale factor, and the procedure is described in detail below. (Note: At the request of a referee, we provide a table of merging statistics in equivolume resolution shells in the Supporting Information. Merging statistics are unsurprisingly large for much of the data beyond 1.1 Å^{-1}, but that sheds no light on the different scales apparent for high- and low-angle data.)

Anharmonic Thermal Motion of Oxygen Atoms. In addition to problems associated with the uncertainty in the scale factor, initial refinements of the X-ray data also indicated substantial contraction (i.e., large radial exponents) of the octopole radial functions on the oxygen atoms. As described

by Sorensen et al.,[65] in their study on tetrafluoroterephthalotnitrile (TFT), this contraction of octopole and dipole functions can indicate the presence of anharmonic thermal motion. That work also demonstrated that third-order coefficients of a Gram-Charlier (GC) expansion can be constructed in terms of dipole and octopole angular functions and that, with care, they could be accurately refined even in the presence of electronic features, despite other studies suggesting that it is not possible to refine both electronic features and third- or fourth-order GC coefficients.[66]

Following the procedure used to identify the effects of anharmonic thermal motion by Sorensen et al.,[65] the constraints involving the oxygen radial parameters were lifted, and a further refinement was carried out. Before removal of the constraint, the oxygen radial parameters refined to values of $\kappa_0 = \kappa_1 = \kappa_2 = 0.988(1)$, and $\alpha_3 = 7.7(5)$ for both atoms. Without the constraints, $\kappa_1 = 2.4(2)$ for O(1) and $\kappa_1 = 8(3)$ for O(2) and $\alpha_3 = 18(6)$ for O(1) and $\alpha_3 = 15(2)$ for O(2), suggesting that the oxygen atoms were undergoing anharmonic motion. On the basis of the resolution limits quoted by Sorensen et al.[65] for the refinement of third-order GC coefficients, the present MNA data is of sufficient resolution to be sensitive to this information for the oxygen atoms. Separation of electronic and thermal motion features is extremely important for the refinement of these parameters and especially for the deconvolution of the electron density from thermal motion. For this noncentrosymmetric space group, it can be achieved by using the electron density model determined by fitting theoretical structure factors in the refinement of third-order GC coefficients.

Self-Consistent Determination of Scale and Thermal Parameters. With problems related to the scale and thermal motion identified, a refinement strategy was devised to take these into consideration. Populations and radial parameters from the refinement against theoretical structure factors were used as the starting density, and the generalized scattering factor model used was identical to that described above, except that the residual minimized was

$$\Delta = \sum_{\mathbf{h}} \left\{ \frac{|F_o(\mathbf{h})| - y_{ext}(\mathbf{h})|F_c(\mathbf{h})|}{\sigma[F_o(\mathbf{h})]} \right\}^2 \qquad (2)$$

An isotropic extinction parameter (type I, Lorentzian distribution[67,68]) and population parameters up to the octopole level for heavy atoms and quadrupole level for hydrogen atoms were refined, but the radial parameters α_0, α_1, and α_2 for hydrogen were not. Position and anisotropic thermal parameters for all heavy atoms and third-order GC coefficients for both oxygen atoms were all refined against the X-ray data with $\sin\theta/\lambda > 0.7$ Å $^{-1}$ and $F \geq 4\sigma(F)$. The *x* and *z* coordinates of O(2) were fixed as before, and the coordinates and ADPs of the hydrogen atoms were fixed at the neutron values.

Because of the underlying philosophy in VALRAY, an overall scale factor cannot be determined at the same time as populations of higher multipole functions, and for this reason, our strategy was an iterative one, summarized in Figure 4. From initial refinements of the data, it was found that the heavy atom ADPs derived from the X-ray and neutron diffraction experiments differed significantly and in a nonsystematic manner, except for the U_{33} component for which the X-ray ADPs systematically overestimated the neutron ADPs by ~8%. Part of this systematic difference can be attributed to slightly different temperatures employed during data collection, as systematic differences are evident between the cell parameters (Table 1). Remaining differences are probably due to a variety of effects

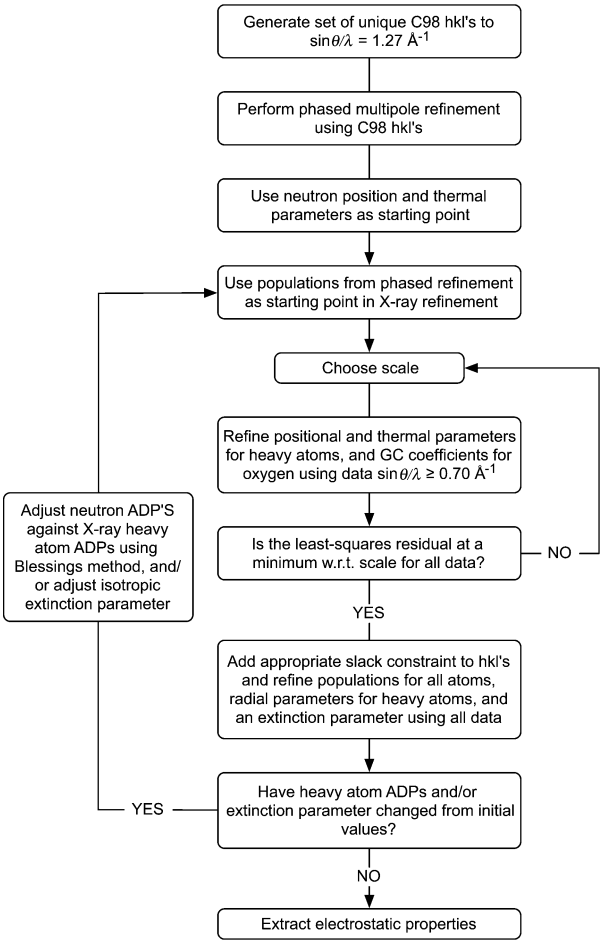

Figure 4. Self-consistent procedure used to determine scale and thermal parameters for the X-ray data.

such as anisotropic extinction in the neutron data, multiple and incoherent scattering. To transfer the neutron ADPs for hydrogen atoms for use in the X-ray refinements, Blessing's procedure was used, as implemented in *UIJXN*.[69] This was performed iteratively (Figure 4), resulting in an rms deviation of 6.24×10^{-4} Å^2 between the final set of heavy atom ADPs determined from the self-consistent refinement of X-ray diffraction data and corrected neutron values. This agreement should ideally be better, but the process yields superior estimates of thermal motion for hydrogen atoms than the assumption of isotropic temperature factors. For comparison, MNA was subjected to the analysis described in detail elsewhere,[70] where ADPs for H atoms were calculated from a rigid-body analysis of X-ray heavy atom ADPs combined with estimates of internal motion derived from an ab initio ONIOM cluster calculation. For hydrogen atoms in MNA, the agreement between the resulting TLS+ONIOM ADPs and corrected neutron values is excellent for almost all atoms, with an overall similarity index of $\bar{S}_{12} = 0.45$, comparable to the result obtained for xylitol, but not as good as for benzene or 1-methyluracil.[70] Most importantly for the present purposes, U_{33} values derived from the neutron diffraction data are reproduced by the TLS+ONIOM method for nearly all hydrogen atoms, and therefore, the thermal motion model adopted for the present charge density analysis can be assumed to be excellent, as closely similar results were obtained by two independent methods. The adjusted neutron diffraction results are considered superior in this case, as the ADPs for hydrogen-bonded H atoms are not biased by minor inadequacies in the theoretical calculation.

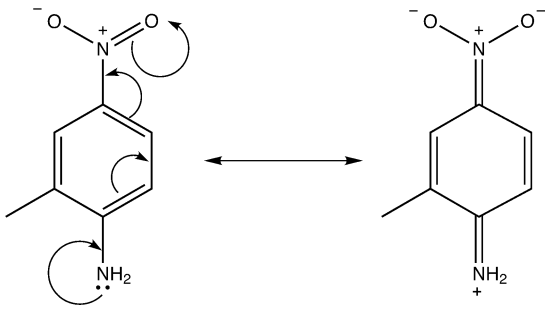

Figure 5. Two different representations of the electronic structure of MNA. Left: normal structure. Right: quinonoid form.

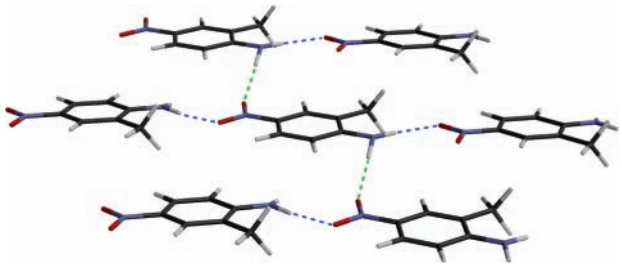

Figure 6. Perspective view of selected molecules in the crystal structure of MNA, indicating the major hydrogen bond interactions present.

Results and Discussion

Crystal Structure. The crystal structure of MNA has been studied on several occasions.[6,15,39] The structure of the molecular units of MNA in the crystal is not significantly different from what would be expected in the gas phase, as the bond lengths and angles compare well with theoretical calculations on an isolated molecule. Of relevance to the present study on molecular polarization are the relative contributions of the two resonance forms shown in Figure 5. If one electron migrated from one end of the molecule to the other, the dipole moment of the molecule would increase dramatically, and the quinonoidal resonance form would dominate; hence, it would be expected that the lengths of alternating bonds in the phenyl ring would differ. Cole and co-workers[16,71,72] have investigated this type of behavior in other NLO materials and rationalized their findings in relation to the second harmonic generation activity of the compounds. Ferguson et al.[39] concluded in their structural study of MNA that the contribution from the quinonoidal form was very small. On the basis of the present neutron diffraction results, the average difference between alternating bond lengths is approximately 0.025 Å, which is small compared with the difference in average C—C and C═C bond lengths[73] of 0.214 Å. The aryl ring and the NO_2 group in the molecule are essentially coplanar, with a torsion angle between them of less than 1°. The NH_2 group is slightly pyramidal, as also observed in 2-methyl-5-nitroaniline (M5NA).[74] The torsion angle between the plane of the ring and the N—H(NA) bond is ~4°, while the torsion angle between the N—H(NB) and the plane of the ring is approximately −13°; hence, both atoms are on the same side of the ring's mean plane, but H(NB) is distorted by a greater amount.

The intermolecular bonding arrangement is complicated, but the two major interactions are both hydrogen bonds. The strongest of these, H(NA)···O(2)′ (shown in Figure 6 by the blue dashed lines), has a contact distance of 2.057(3) Å and links molecules of MNA head to tail, forming hydrogen-bonded chains. This interaction is almost in the same plane as the molecule and explains why H(NA) is not significantly removed from the molecular plane. The other interaction is a weaker hydrogen bond, H(NB)···O(1)″ (shown in Figure 6 by the green dashed lines), with a contact distance of 2.279(3) Å, and this links different chains together. Not shown in the simplified depiction in Figure 6 is that each of the chains are also linked above and below the molecular plane to adjacent chains, forming a three-dimensional framework structure,[39] with the interaction between the different layers (green dashed lines) forcing H(NB) to deviate from the mean molecular plane. (O(2)′ and O(1)″ denote atoms in two different adjacent molecules.)

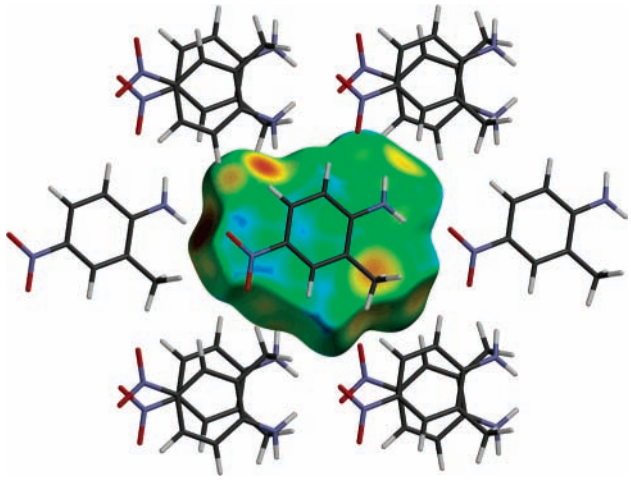

Figure 7. Hirshfeld surface for MNA, with the distance from the surface to the closest nucleus ouside the surface (d_e) mapped on the surface.

A novel method for exploring and discussing intermolecular interactions in molecular crystals is by the use of the Hirshfeld surface.[75,76] Figure 7 portrays a Hirshfeld surface for MNA surrounded by a cluster of neighboring molecules; the property mapped on the surface is the distance from the surface to the closest atom (d_e), with red being closest and blue being farthest from the surface.[77] Hydrogen bonds are identified as flat red spots on the surface; the red patch on the far left of the surface identifies the H(NA)···O(2)′ contact. The other hydrogen bond, H(NB)···O(1)″, appears as the orange patch on the upper left section of the surface in Figure 7. The remaining yellow and orange patches on the Hirshfeld surface correspond to other close intermolecular contacts in the crystal. The yellow and orange regions around the perimeter of the surface result from close H···H and C—H···O interactions, and those on the upper (and lower) faces of the surface are due largely to C—H···π contacts made by the out-of-plane methyl hydrogen atoms. Another feature highlighted in Figure 7 is the significant amount of $\pi-\pi$ stacking, shown by the overlapping molecules.

The fingerprint plot[77,78] for MNA (Figure 8) shows the two characteristic hydrogen bond donor−acceptor spikes from the N—O···H—N interactions. The different hydrogen bonds cannot be distinguished on the plot, as the features due to the slightly longer interribbon contacts lie in the upper part of each spike, because the ratio of d_e/d_i is the same for both contacts. The large diffuse green region at $d_e = d_i = 1.8$ Å indicates a large contribution from $\pi-\pi$ stacking, and the small wings on either side of the fingerprint plot are indicative of weak C—H···π interactions, in this case involving the methyl hydrogen atoms. From the Hirshfeld surface and fingerprint plot, the major interactions in the crystal are readily identified and reveal nothing unusual in the intermolecular packing arrangement.

Theoretical Electron Density. The Hartree−Fock *CRYSTAL98* deformation electron density (the difference between the crystal density and sum of spherical atoms) in the MNA

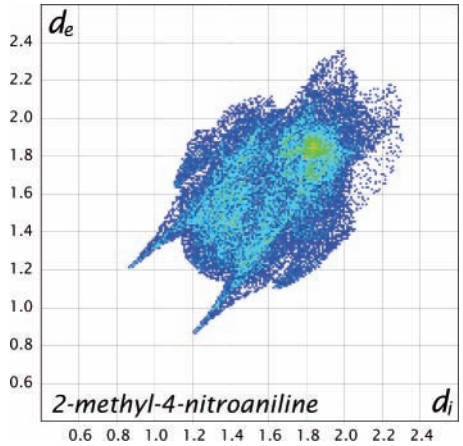

Figure 8. Fingerprint plot for MNA.

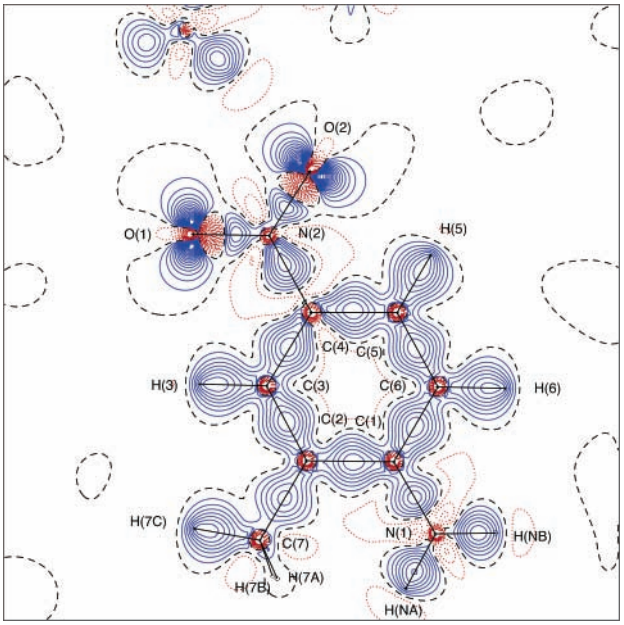

Figure 9. Theoretical deformation density of MNA ($\rho_{C98}(\mathbf{r}) - \rho_{IAM}(\mathbf{r})$) in the plane of C(1), C(4), and C(5); contour styles and intervals as in Figure 2.

molecular plane is shown in Figure 9. Typical features are evident in all bonds, and it is notable that one lone-pair peak of O(2) is directed toward H(NA) in an adjacent molecule (top of Figure 9). Features in this map are compared with those from the experimental electron density below. The theoretical interaction density (the difference between the crystal density and that obtained from the superposition of noninteracting molecular densities), Figure 10, is very similar to that published earlier for *p*-nitroaniline.[19] In both, the electron density is locally polarized, with local dipoles pointing in the same general direction. These features are also consistent with earlier theoretical studies on ice VIII, formamide, and urea[50] and are characteristic of hydrogen bonding. The best example for MNA is seen for the in-plane hydrogen bond between O(2) and H(NA)′, where the electron density in the donor N−H(NA) bond and around the O(2) acceptor atom has been substantially polarized. Also of interest is the unexpected dipolar feature around H(6), which clearly differs from the pattern observed for the other hydrogen atoms bonded to the phenyl ring. This feature resembles that at H(NA), although less pronounced, and indicates that H(6) is involved in a weak C−H···X hydrogen bond. Inspection of Figure 7 confirms this to be the case, the interaction being with O(1), as shown by a yellow region on the upper left of the Hirshfeld surface, between the features due to the two major hydrogen bonds.

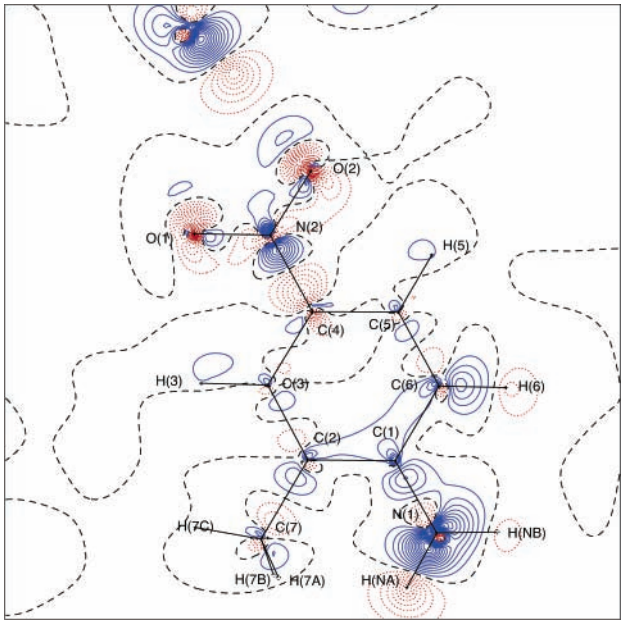

Figure 10. Theoretical interaction density for MNA ($(\rho_{C98}(\mathbf{r}) - \rho_{MOLSPLIT}(\mathbf{r}))$; mapping plane and contour styles as in Figure 2, with contour interval of 0.01 e Å^{-3}.

TABLE 2: Radial Scaling Parameters Derived from Refinements against Experimental and Theoretical Structure Factors

	experiment		theory	
	κ	α (au)	κ	α (au)
		oxygen		
	0.986(2)	4.5(4)	0.9871(2)	4.79(5)
		nitrogen		
N(1)	0.983(3)	3.29(10)	0.9868(4)	3.401(12)
N(2)	0.979(2)	3.24(7)	0.9739(3)	3.274(7)
		carbon		
C(1)	0.995(4)	3.12(3)	0.9959(6)	3.144(4)
C(2)	1.007(4)	3.12(3)	0.9947(5)	3.144(4)
C(3)	1.000(4)	3.12(3)	0.9921(6)	3.144(4)
C(4)	1.013(4)	3.12(3)	1.0081(5)	3.144(4)
C(5)	1.008(4)	3.12(3)	0.9886(6)	3.144(4)
C(6)	1.014(4)	3.12(3)	0.9966(5)	3.144(4)
C(7)	1.010(4)	2.74(8)	0.9925(7)	3.079(8)
		hydrogen		
		2.269		2.269(2)

Experimental Electron Density. The procedure described above was carried out to yield the final experimental model electron density for MNA. Refinement statistics and other details from the refinement are listed in Table 1. The electron density in the bonding regions of the residual Fourier map are largely random and small, with the exception of small peaks at heavy atoms of magnitude ~0.2 e Å^{-3}. The extinction correction deserves comment: there is a significant correction of ~10% to $|F|$ for the $(\bar{1}12)$ reflection, with the next largest correction being ~4% for the (200) reflection; therefore, the effect is very small for this set of data. Comparing electronic parameters from multipole refinements is not always straightforward, as they depend on implicit normalization factors and the coordinate system used. In contrast, radial scaling parameters are comparable, as they are invariant to the coordinate system used, and Table 2 compares the experimental results with values obtained

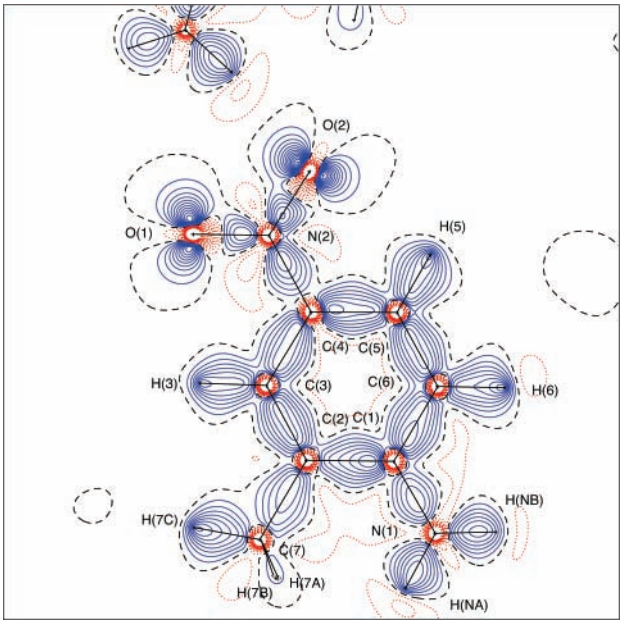

Figure 11. Static experimental deformation density, $\rho_c(\mathbf{r}) - \rho_{IAM}(\mathbf{r})$; mapping plane, contour styles, and intervals as in Figure 2.

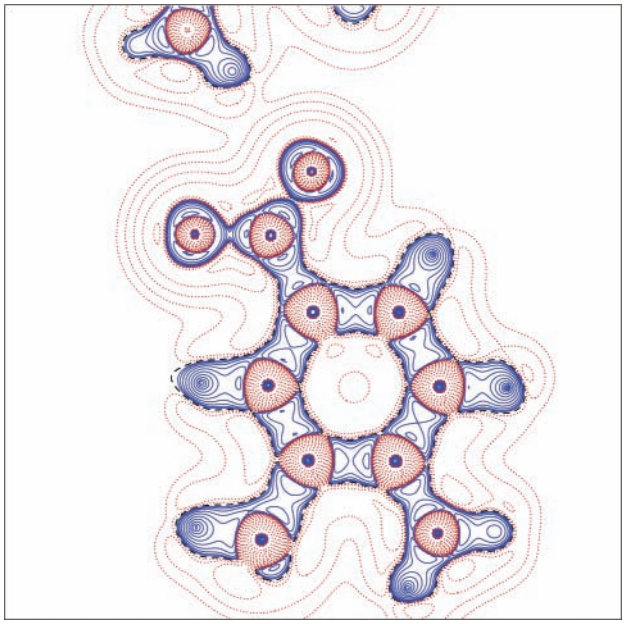

Figure 12. Negative Laplacian of MNA based on experimental static electron density. Mapping plane as in Figure 2, and contours are at intervals of $\pm 2^n$ e Å^{-5}, $n \geq 0$. Solid contours indicate negative $\nabla^2\rho(\mathbf{r})$ (charge concentration) and dashed contours positive $\nabla^2\rho(\mathbf{r})$ (charge depletion).

from the fit to theoretical structure factors. The scaling parameters for the radial functions composed of products of localized orbitals, κ (Table 2), are all very close to unity, and experiment and theory agree well. Scaling parameters for the single-exponential functions, α, are also in good agreement with those derived from theory, and although the present radial functions differ from the conventional choices, the exponents obtained are in agreement with results from other model studies.[50,79,80] The static experimental deformation density of MNA shown in Figure 11 is in excellent agreement with the theoretical deformation density (Figure 9). The magnitudes and shapes of the deformations are all consistent with what is expected for the functional groups present in the compound, and we note that the present result is markedly superior to the deformation density maps reported by Howard et al.[15] (Figure 3 in that work), especially the features around the hydrogen atoms. The agreement between these two maps, the refinement statistics (Table 1), and a largely featureless residual map all indicate that the present model represents an excellent fit to the experimental X-ray data.

Topological Analysis of the Experimental Electron Density. On the basis of Bader's quantum theory of atoms in molecules (QTAM),[81] the Laplacian of the electron density, $\nabla^2\rho(\mathbf{r})$, indicates where charge is locally concentrated and depleted, in a manner independent of any reference density, and topological analysis of the electron density has become the preferred choice for highlighting features of the electron distribution from a multipole refinement.[82] The original charge density study on MNA was among the first experimental studies to map the Laplacian to analyze the model electron density distribution. Figure 12 shows the experimental negative Laplacian for MNA, highlighting the features of the electron density in a similar way to the deformation density (Figure 11). Blue regions show where charge is concentrated between atoms in covalent bonds, and other important features include the core structure evident for C, N, and O and the lone-pair density on oxygen, features which are consistent with other work involving nitro groups.[15,37] As discussed by Bader,[81] details of chemical bonding can be characterized by the topological features of $\rho(\mathbf{r})$ at bond critical points (BCPs), especially $\rho(\mathbf{r}_c)$, the three eigenvalues of the matrix of second derivatives, λ_1, λ_2, and λ_3, and the Laplacian, $\nabla^2\rho(\mathbf{r}_c) = \lambda_1 + \lambda_2 + \lambda_3$.

Bond critical point properties derived from the experimental electron density for MNA are summarized in Table 3 for the *CRYSTAL98* electron density, the electron density obtained from multipole refinement against *CRYSTAL98* structure factors, and the experimental model electron density. Although topological analysis of experimental model electron densities has become the norm in modern charge density analysis, all too often these quantities are tabulated in an uncritical fashion for all bond types (intramolecular and intermolecular) in the crystal, despite the fact that there is ample evidence that for some bond types there are large systematic deficiencies associated with results obtained from multipole models. For this reason, Table 3 reports mostly quantities averaged over similar bond types in order to make the results more readily accessible (full details for all bonds are provided in the Supporting Information). The best experimental reference for MNA is its isomer 2-methyl-5-nitroaniline (M5NA), for which all the bond critical point properties were reported from a combined neutron and X-ray charge density study;[56] our present results are consistent with the experimental and theoretical results reported for M5NA. (Note: In the M5NA study, the theoretical values for $\nabla^2\rho(\mathbf{r}_c)$ are clearly incorrect for the N−O bond. Neither a *CRYSTAL98* calculation on M5NA nor a free molecule calculation gives values comparable with the published results for M5NA, while theoretical results from our calculations on M5NA are in close agreement with the present theoretical results for MNA.) For MNA (Table 3), general agreement is observed between experiment and theory (both multipole fitted and directly from the periodic calculation) for $\rho(\mathbf{r}_c)$, and for all bond types. However, the same is not true for the Laplacian, where the multipole fit to either experiment or theory yields values that are different from those computed directly from the Hartree−Fock density for all except a few bond types. The origin of this discrepancy is readily identified from inspection of the eigenvalues, λ_1, λ_2, and λ_3. Systematic differences are observed between the theoretical calculation and the multipole model for λ_3, with the eigenvalue of the Hessian

TABLE 3: Mean Bond Critical Point Properties for Sets of Unique Bond Types in MNA[a]

bonds	$\rho(\mathbf{r})$ (e Å^{-3})	$\nabla^2\rho(\mathbf{r})$ (e Å^{-5})	λ_1	λ_2	λ_3
C(1)−C(2), C(2)−C(3), C(3)−C(4), C(4)−C(5), C(5)−C(6), C(6)−C(1)	2.09(14)	−17(4)	−16.5(7)	−12.7(5)	12.4(4)
	2.10(5)	−17.8(8)	−16.6(6)	−12.9(4)	11.8(3)
	2.17(5)	−27.0(9)	−16.6(5)	−13.2(3)	2.7(4)
C(2)−C(7)	1.70(4)	−10(3)	−11.7	−10.4	11.6
	1.72	−11.6	−11.8	−11.1	11.3
	1.80	−19.4	−12.7	−12.2	5.4
C(1)−N(1)	2.18(13)	−21.1(10)	−17.5	−13.8	10.1
	2.27	−23.5	−19.1	−16.5	12.1
	2.19	−19.2	−17.0	−16.7	14.5
C(4)−N(2)	1.89(9)	−15.4(20)	−13.8	−11.2	9.6
	1.83	−16.5	−13.5	−9.6	6.6
	1.77	−2.8	−12.3	−8.8	18.3
N(2)−O(1), N(2)−O(2)	3.26(10)	−9(7)	−29.5(8)	−26.8(1)	48.0(17)
	3.18(3)	−7.7(1)	−28.3(3)	−26.1(1)	46.7(4)
	3.33(3)	−28.1(9)	−30.5(3)	−27.1(4)	29.5(3)
N(1)−H(NA), N(1)−H(NB)	2.3(3)	−37(7)	−31.6(2)	−29.2(6)	23.6(23)
	2.25(7)	−33.3(16)	−30.4(9)	−28.3(11)	25.0(7)
	2.35(7)	−44.0(22)	−34.2(17)	−32.5(16)	22.7(10)
C(3)−H(3), C(5)−H(5), C(6)−H(6), C(7)−H(7A), C(7)−H(7B), C(7)−H(7C)	1.90(18)	−20.7(35)	−18.1(10)	−17.1(9)	14.4(16)
	1.89(5)	−20.0(15)	−17.8(12)	−17.1(10)	14.8(10)
	1.97(5)	−28.4(19)	−18.4(10)	−18.1(13)	8.1(4)
H(NA)···O(2)′	0.11(4)	1.0(3)	−0.7	−0.7	2.4
	0.13	1.5	−0.7	−0.7	2.9
	0.12	1.7	−0.6	−0.5	2.7
H(NB)···O(1)″	0.08(2)	1.0(2)	−0.4	−0.3	1.7
	0.06	1.0	−0.3	−0.2	1.5
	0.07	1.1	−0.3	−0.2	1.6

[a] First row: experimental results. Second row: phased multipole fit to theoretical structure factors. Third row: periodic Hartree−Fock calculation. Figures in parentheses indicate the range of results, experimental esds, or a combination of the two.

corresponding to the curvature along the bond path. In the literature, this has been attributed to the limited flexibility of the radial functions used in the multipole model, as well as basis set and electron correlation effects,[83−85] although it has been recently discovered that it may also be due to the different behavior of Gaussian and Slater-type radial functions in the vicinity of the bond.[86] However, it seems clear from recent comparisons between theory and experiment for C−O,[37] C−F,[87,88] N−O,[37,89] and C−S[90] bonds that this discrepancy is especially common for polar bonds, where the Laplacian is rapidly varying along the internuclear vector, and the location of the BCP can differ greatly between experiment and theory. This is certainly the case for the present MNA results for C−N, N−O, and C−H bonds. The curvatures for the amino N−H bonds and the intermolecular hydrogen bonds are well-reproduced in all circumstances.

The topological analysis of the crystal Hartree−Fock electron density yields a number of (3, −1) critical points in the intermolecular region, in addition to the two conventional hydrogen bonds listed in Table 3. There are four C−H···O interactions (two involving phenyl hydrogens, the strongest of which is the H(6)···O(1) contact identified from the theoretical interaction density, and two involving methyl hydrogens), one C−H···C interaction involving a methyl hydrogen, and six H···H interactions. These weak BCPs are rarely discussed in experimental charge density studies as they occur where the electron density is extremely flat, and their properties are largely dictated by the procrystal electron density;[91] for those reasons, we do not report any experimental results for MNA. However, we note that the importance of H···H interactions in molecules and crystals has been recently discussed in detail by Matta et al.[92]

Atomic Charges and Molecular Dipole Moment. As discussed in the Introduction, the polarization of electron density induced in a molecule in the crystal can be attributed to the crystal field and intermolecular bonding, and this effect can be analyzed in terms of the atomic charges and dipole moment of the molecule. An important objective of the present study was the verification (or otherwise) of the large increase of the molecular dipole moment in the crystal, relative to the free molecule, which was the key finding of the previous study by Howard et al.[15] The QTAM net charges obtained from the experimental electron density, as well as theoretical Hartree−Fock densities for the crystal and a superposition of noninteracting molecules, are listed in Table 4 for all atoms, as well as for specific functional groups. There is general agreement among all three sets of charges that the most highly charged atoms are in the $-NO_2$ and $-NH_2$ groups. The rms difference between the "crystal" and "molecules" charges is only 0.04 e, and that between the experimental and theoretical "crystal" charges is 0.17 e (although no estimates of esds can be given at present for the experimental results, it is likely that this latter rms difference is on the same order as typical esds). The systematic differences between the "crystal" and "molecules" charges hints at the degree of polarization of the electron distribution due to the intermolecular interactions: the $-NO_2$ group becomes slightly more negative (by 0.07 e), and the $-NH_2$ group slightly more positive (also by 0.07 e). Thus, ∼0.07 e is transferred from one end of the molecule to the other (the N(1)−N(2) separation is ∼5.6 Å), suggesting a dipole moment enhancement of ∼1.9 D (this estimate ignores changes in the atomic dipoles). At a more detailed level, the H atom involved in the shortest hydrogen bond (H(NA)···O(2)′ = 2.057 Å) becomes more positive by 0.07 e, while that involved in the longer hydrogen bond (H(NB)···O(1)′ = 2.279 Å) loses only 0.04 e. It is also noteworthy that H(6), which participates in a weak C−H···O interaction, loses 0.04 e, the only ring H atom to do so.

Molecular dipole moments for MNA based on a number of partitioning schemes applied to the present experimental and

TABLE 4: Atomic and Group Charges from QTAM Partitioning of the Electron Density[a]

atom	experimental	crystal	molecules
O(1)	−0.45	−0.59	−0.54
O(2)	−0.35	−0.58	−0.54
N(1)	−1.27	−1.49	−1.45
N(2)	0.16	0.30	0.28
C(1)	0.20	0.45	0.43
C(2)	0.09	0.18	0.14
C(3)	−0.12	0.02	0.04
C(4)	0.11	0.21	0.27
C(5)	−0.01	0.01	0.06
C(6)	−0.14	0.20	0.18
C(7)	−0.07	0.22	0.22
H(NA)	0.58	0.53	0.46
H(NB)	0.45	0.50	0.46
H(3)	0.20	0.06	0.06
H(5)	0.17	0.06	0.07
H(6)	0.16	0.03	−0.01
H(7A)	0.11	−0.03	−0.05
H(7B)	0.01	−0.05	−0.05
H(7C)	0.17	−0.04	−0.03
	groups		
NO_2	−0.64	−0.87	−0.80
NH_2	−0.24	−0.46	−0.53
CH_3	0.22	0.10	0.09
ring	0.66	1.22	1.24

[a] Experimental: model density derived from multipole refinement against experimental structure factors. Crystal: theoretical crystal Hartree−Fock calculation. Molecules: superposition of noninteracting Hartree−Fock molecular densities.

TABLE 5: Dipole Moment Magnitudes (debye) from Various Theoretical and Experimental Methods[a]

	$\|\mu\|$	x	y	z
	experimental			
QTAM	11.3	−0.81	0.10	−0.58
Hirshfeld surface	9.8	−0.86	0.06	−0.50
multipole	12.4(13)	−0.8(2)	0.1(1)	−0.5(1)
	Crystal 98			
QTAM	11.7	−0.85	0.27	−0.45
Hirshfeld surface	9.3	−0.85	0.28	−0.45
	phased multipole fit to theoretical structure factors			
QTAM	11.5	−0.85	0.24	−0.46
Hirshfeld surface	10.0	−0.87	0.22	−0.44
multipole	11.7	−0.85	0.24	−0.46
	sum of noninteracting molecular densities			
QTAM	9.0	−0.85	0.28	−0.45
Hirshfeld surface	6.9	−0.84	0.28	−0.46
	geometry optimized free molecule using a DZP basis set			
HF	6.9			
MP2	7.1			
	experimental measurements in solution[107]			
benzene	6.40			
dioxane	6.98			

[a] Direction cosines are also given for the theoretical and experimental crystal results, with the *x* axis parallel to *a* and the *z* axis perpendicular to the *ab* plane.

theoretical electron densities, as well as from other sources, are reported in Table 5. The maximum difference between dipole moment directions, from experiment and theory and for either the QTAM or Hirshfeld surface integration results, is approximately 19° and is due largely to the charge buildup on the methyl carbon atom, C(7), relative to that observed in the theoretical calculation (Table 4). The only dipole moment esd given in the table is for the multipole result, and it represents a lower bound of the true experimental error, because systematic errors, especially those associated with scaling the data and the use of a restraint, are not taken into account. Nevertheless, the value derived directly from the multipole refinement, 12.4(13) D, is much smaller than the previous result reported by Howard et al.[15] It is also close to the narrow range of QTAM results for the crystal (11.3−11.7 D) which, compared with the result of 9.0 D for the QTAM partitioning of the sum of molecules electron density, suggests a dipole moment enhancement of 2.3−2.7 D (26−30%). Similarly, estimates based on integration over Hirshfeld surfaces[93] range from 9.3 to 10.0 D for the molecule in the crystal, compared with 6.9 for the superposition of molecules, an enhancement of 2.6−3.1 D (35−45%). As observed elsewhere,[93] Hirshfeld surface estimates of dipole moments are systematically smaller than QTAM results but yield similar estimates of dipole moment enhancement. Results for isolated molecules range from 6.4 to 7.1 D.

It is clear that the dipole moment derived from the present careful multipole modeling of X-ray diffraction data is entirely consistent with the theoretical calculations and is significantly smaller than previous estimates. It still represents a considerable enhancement over free molecule calculations or experimental measurements in solution and is consistent with recent work by some of us,[93] which has shown that enhancements of the dipole moment for hydrogen-bonded molecular crystals are typically (but not always) on the order of 30−40%.

Electric Field Gradients at Hydrogen Nuclei. Electric field gradients (EFGs) for hydrogen atoms are an excellent measure of the quality of a charge density refinement, as they can shed light on the accuracy of both the thermal motion model and the local quadrupole deformations. Importantly, they can be obtained independently from nuclear quadrupole resonance (NQR) experiments. The EFG tensor is conventionally cast in traceless form such that $|\nabla E_{xx}| \leq |\nabla E_{yy}| \leq |\nabla E_{zz}|$, and deuterium quadrupole coupling constants (DQCCs) can be calculated from the following expression[94,95]

$$DQCC\ (\mathrm{kHz}) = \frac{e^2 Q}{h} \nabla E_{zz} = 99.6(5)[-\nabla E_{zz}\ (\mathrm{e\ \AA^{-3}})] \quad (3)$$

EFGs can also be obtained from a multipole refined electron density,[96] but the number of studies reporting these quantities is small.[97] Because this method does not rely on the coupling between the nuclear quadrupole moment and the electric field gradient, it could in principle be obtained for all elements. However, even X-ray diffraction data of high quality and resolution are unable to reveal the very sharp deformations of the core electrons, which are often the major contributors to the EFG. Hydrogen is a special case, as it does not possess core electrons; but because the EFGs at hydrogen nuclei are dominated by monopoles on close atoms and the quadrupoles on the hydrogen atom,[97] it is important that all quadrupole deformations are refined on the hydrogen atoms. This requires the motion of the hydrogen atoms to be modeled anisotropically, which excludes most present charge density studies on organic molecules.

DQCCs and hence EFGs are sensitive to the bonding environment of the atom in question, and particularly for atoms in hydrogen-bonded environments.[98] For this reason, values obtained from a multipole refinement are only comparable with solid-state NQR measurements or theoretical calculations of the bulk. Compounds for which solid-state NQR experiments have been carried out include benzene[99−101] and a range of amino acids.[102] Accurate charge density studies have been performed on benzene,[94] glycine,[103] and L-alanine,[104] and the EFG results compared with values obtained from NQR experiments. The DQCCs derived from the electric field gradient for these

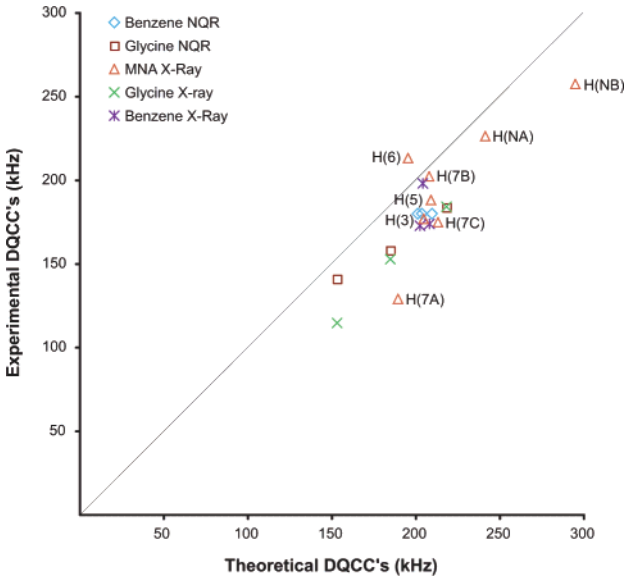

Figure 13. Comparison between theoretical and experimental DQCCs for benzene, glycine, and MNA (labeled data points). The line of unit slope is for reference.

compounds showed good agreement with the NQR measurements, and it is probably not coincidental that all of those charge density studies paid detailed attention to the anisotropic modeling of hydrogen atom thermal motion. Unfortunately, DQCCs have not been experimentally determined for MNA, but experimental results for glycine and benzene can be used to gauge the accuracy of the DQCCs derived from the present model electron density and to identify any systematic trends between the experimental results and those obtained from the crystal Hartree−Fock calculations.

Figure 13 compares crystal Hartree−Fock estimates of DQCCs for benzene, glycine, and MNA with experimental NQR and X-ray diffraction results. The figure reveals that trends between theoretical and X-ray derived EFGs for MNA are in line with those observed between theory and experiment (both diffraction and NQR) for benzene and glycine. NQR results for benzene and glycine vary almost linearly with theory, but there are some obvious inconsistencies between DQCCs derived from the X-ray data and the theoretical data. For both MNA and benzene X-ray results, there is an outlier in the group of phenyl hydrogen atoms, for which the DQCC is overestimated. In the benzene study,[94] it was concluded that the outlier may be caused by a C−H···π contact and not observed in the NQR experiment because the temperature of that study (263 K) allowed fast rotation of the benzene ring, making all hydrogen atoms appear equivalent. The present theoretical calculation does not support that conclusion. For MNA, the outlier, H(6), has a trace of the ADP tensor that is >10% larger than for the other two ring H atoms, and while the difference is smaller, H(2) in benzene (the outlier for DQCCs) also has the largest trace of the ADP tensor. This suggests that the problems are in part related to the description of thermal motion for each of these atoms.

EFGs and DQCCs for all H atoms in MNA are reported in Table 6; no esds are given, as this capability has not yet been implemented into any charge density refinement program. The large difference between the DQCCs for the amino hydrogen atoms in MNA, H(NA), and H(NB) and observed for both experimental and theoretical results reflects the difference between hydrogen bond contacts for these atoms. Hydrogen bond formation reduces the magnitude of the DQCCs;[98] hence, the lower DQCC for H(NA) relative to that of H(NB) is directly related to the hydrogen bond strengths. X-ray-derived DQCCs appear never to have been reported previously for methyl hydrogen atoms. There are several reasons for this, the foremost being the lack of experimental results for these functional groups. For example, NQR measurements of amino acids by Hunt and Mackay[102] do not report them, as the exchange process used to deuterate the compounds does not work well for the less acidic hydrogen atoms; hence, the DQCCs cannot be measured. A practical issue for the determination of EFGs from X-ray diffraction data at methyl hydrogen nuclei is the relatively large vibrational amplitudes of methyl hydrogen atoms, making accurate deconvolution of thermal motion vital. For MNA, the theoretical values can be compared only with the X-ray experimental results, and the agreement is reasonable for H(7B) and H(7C), but H(7A) is an extreme outlier. The reason is in part related to the longer C−H bond length for this atom (1.089 Å, compared with 1.080 and 1.085 Å for the other methyl−H bonds), although it is likely that much of the difference can be attributed to the modeling of thermal motion for the entire methyl group.

TABLE 6: Theoretical and Experimental EFGs and Deuteron Quadrupole Coupling Constants for Hydrogen Atoms in MNA

	∇E_{zz} (e Å^{-3})		DQCC (kHz)	
	experiment	theory	experiment	theory
H(3)	−1.79	−2.08	179	207
H(5)	−1.90	−2.12	189	211
H(6)	−2.16	−1.98	215	197
H(NA)	−2.29	−2.45	228	245
H(NB)	−2.61	−3.01	260	300
H(7A)	−1.29	−1.92	129	191
H(7B)	−2.04	−2.11	203	210
H(7C)	−1.76	−2.17	176	216

One final point is relevant in the comparison of EFG results from different experimental measurements. Great care was taken in the calculation of EFGs for benzene[94] such that the chosen coordinate system was the same as that used in the NQR measurements. In general, however, it is the principal component of the EFG tensor with the largest magnitude that is compared with the NQR result, and the error introduced by diagonalization of the X-ray derived EFG tensor is large, since the tensor components computed from the multipole model all have inherent experimental errors, which are likely to be substantial. In the present case, the EFG tensor has been diagonalized for both the theoretical and experimental results, which may lead to some ambiguity in the comparison.

Concluding Remarks

This study was motivated by a desire to critically reexamine the validity of the conclusion from an earlier experimental charge density analysis, in which the molecular dipole moment of MNA in the crystal is substantially enhanced due to a combination of strong intermolecular interactions and crystal field effects. X-ray and neutron diffraction data have been carefully measured at 100 K and supplemented with ab initio crystal Hartree−Fock calculations to provide the best possible basis for a new charge density analysis on the crystal. Considerable care was taken in measurement and reduction of the experimental data to exclude as many systematic errors as possible and, in the subsequent analysis, to identify all possible sources of error and account for their effects on the resulting model electron density. The electron density derived from a fit to theoretical structure factors assisted in the determination of the scale, anisotropic displacement parameters, and third-order

Gram−Charlier coefficients for some atoms. All experimental and theoretical evidence leads us to conclude that the dipole moment enhancement for MNA in the crystal is nowhere near that reported previously and is only on the order of 30−40% (∼2.5 D). The huge apparent enhancement reported by Howard et al.[15] was most likely due to the variability of the phases for this polar acentric space group, uncertainty in the experimental scale factor for the X-ray diffraction data, as well the isotropic description of the thermal motion of H atoms.

Experimental deformation electron density maps, bond critical point data, electric field gradients at hydrogen nuclei, and atomic and group charges all agree well with theoretical results and trends. Modeling of the motion of hydrogen atoms as anisotropic, periodic ab initio calculations, and data quality are all aspects of this study that represent a considerable improvement over previous work. Whether the issues identified in this study are due to systematic problems in the X-ray data collection and reduction or large relative errors on the high-angle data is presently unknown. Although it might appear that the present model experimental electron density relies heavily on the ab initio results, the projected ab initio electron density parameters were used only to determine the scale, to give a more realistic estimate of the thermal motion model (i.e., anharmonicity for the oxygen atoms) and to determine the most appropriate radial parameters for the hydrogen multipoles (and these are usually fixed at an arbitrary value in other studies.[53,105]); all other parameters in the experimental model electron density were determined by the experimental data. Other aspects of the procedure, such as fixing the scale factor at early stages of the refinement, are also a common practice when other multipole refinement packages are used.

The fact that the present results are clearly at variance with the conclusions of Howard et al., whose study has become the archetype for large dipole moment enhancements in molecular crystals, leads us to question the validity of all such examples in the literature. Of all cases where substantial (>100%) dipole moment enhancements have been observed, only the studies on *p*-amino-*p′*-nitrobiphenyl[26] and MNA[15] report problems with model dependency, although we suspect it is an important factor in most studies of this kind. In addition, almost all such studies model hydrogen atom thermal motion as isotropic, and the importance of this point is largely neglected among the charge density community. In the absence of neutron diffraction data, given the relatively modest CPU time taken by an ab initio calculation, even for moderately large systems, and given the availability of utilities such as XDVIB,[106] and the ease with which rigid body analysis can be carried out, there would seem to be little reason for not using ADPs for hydrogen atoms,[70] especially where a property such as the molecular dipole moment is under investigation. Hydrogen atoms, like all other atoms, contribute to the overall valence density and are free to accept or donate electron density. They almost exclusively lie on the periphery of a molecule, where they can make a large contribution to the dipole moment.

Acknowledgment. This research is supported by the Australian Research Council. A.E.W. is grateful for the receipt of an Australian Postgraduate Award, as well as a Postgraduate Research Award from the Australian Institute of Nuclear Science and Engineering, which funded his Ph.D. studies. We are indebted to Prof. Masaru Tachibana (Yokohama City University, Japan) for his kind donation of the crystal used for neutron diffraction and to Dr. Josh McKinnon (UWA) for his assistance with the graphics.

Supporting Information Available: Positional and anisotropic displacement parameters for all atoms, Gram−Charlier coefficients for oxygen atoms, bond critical point properties (from experiment, phased multipole fit to theoretical structure factors, and from periodic Hartree−Fock calculation), and residual Fourier electron density map, $|F_o| - |F_c|$. This material is available free of charge via the Internet at http://pubs.acs.org.

References and Notes

(1) Bosshard, C.; Sutter, K.; Prêtre, P.; Hulliger, J.; Flörsheimer, M.; Kaatz, P.; Günter, P. *Organic Nonlinear Optical Materials*; Gordon and Breach: Basel, 1995.

(2) Prasad, P. N.; Williams, D. J. *Introduction to nonlinear optical effects in molecules and polymers*; Wiley: New York, 1991.

(3) Sutherland, R. L. *Handbook of Nonlinear Optics*; Marcel Dekker: New York, 1996.

(4) Zyss, J. *Molecular nonlinear optics. Materials, physics and devices*; Academic Press: New York, 1994.

(5) Levine, B. F.; Bethea, C. G.; Thurmond, C. D.; Lynch, R. T.; Bernstein, J. L. *J. Chem. Phys.* **1979**, *50*, 2523.

(6) Lipscomb, G. F.; Garito, A. F.; Nerang, R. S. *J. Chem. Phys.* **1981**, *75*, 1509.

(7) Lipscomb, G. F.; Garito, A. F.; Nerang, R. S. *Appl. Phys. Lett.* **1981**, *38*, 663.

(8) Ho, E. S. S.; Iizuka, K.; Freundorfer, A. P.; Wah, C. K. L. *J. Appl. Phys.* **1991**, *69*, 1173.

(9) Tokura, Y.; Kurita, A.; Koda, T. *Phys. Rev. B* **1985**, *31*, 2588.

(10) Morita, R.; Ogasawara, N.; Umegaki, S.; Ito, R. *Jpn. J. Appl. Phys.* **1987**, *26*, L1711.

(11) Sugihara, O.; Toda, T.; Ogura, T.; Kinoshita, T.; Sasaki, K. *Opt. Lett.* **1991**, *16*, 702.

(12) Paturle, A.; Graafsma, H.; Boviatsis, J.; Legrand, A.; Restori, R.; Coppens, P.; Kvick, Å.; Wing, R. M. *Acta Crystallogr.* **1989**, *A45*, FC25.

(13) Paturle, A.; Graafsma, H.; Sheu, H.-S.; Coppens, P.; Becker, P. *Phys. Rev. B* **1991**, *43*, 14683.

(14) Graafsma, H.; Paturle, A.; Wu, L.; Sheu, H. S.; Majewski, J.; Poorthuis, G.; Coppens, P. *Acta Crystallogr., Sect. A* **1992**, *48*, 113.

(15) Howard, S. T.; Hursthouse, M. B.; Lehmann, C. W.; Mallinson, P. R.; Frampton, C. S. *J. Chem. Phys.* **1992**, *97*, 5616.

(16) Cole, J. M. *Philos. Trans. R. Soc. London, Ser. A* **2003**, *361*, 2751.

(17) Puig-Molina, A.; Alvarez-Larena, A.; Piniella, J. F.; Howard, S. T.; Baert, F. *Struct. Chem.* **1998**, *9*, 395.

(18) Spackman, M. A.; Byrom, P. G. *Acta Crystallogr., Sect. B* **1997**, *53*, 553.

(19) Coppens, P.; Volkov, A. *Acta Crystallogr., Sect. A* **2004**, *60*, 357.

(20) Koritsanszky, T. S.; Coppens, P. *Chem. Rev.* **2001**, *101*, 1583.

(21) Ritchie, J. P. *Chem. Phys. Lett.* **2004**, *387*, 243.

(22) Volkov, A.; Gatti, C.; Abramov, Y.; Coppens, P. *Acta Crystallogr., Sect. A* **2000**, *56*, 252.

(23) Gopalan, R. S.; Kulkarni, G. U.; Rao, C. N. R. *ChemPhysChem* **2000**, *1*, 127.

(24) Kulkarni, G. U.; Kumaradhas, P.; Rao, C. N. R. *Chem. Mater.* **1998**, *10*, 3498.

(25) Munshi, P.; Row: T. N. G. *Acta Crystallogr., Sect. B* **2002**, *58*, 1011.

(26) Volkov, A.; Wu, G.; Coppens, P. *J. Synchrotron Rad.* **1999**, *6*, 1007.

(27) Ferenczy, G. G.; Csonka, G. I.; Naray-Szabo, G.; Angyan, J. G. *J. Comput. Chem.* **1998**, *19*, 38.

(28) Munn, R. W. *J. Chem. Phys.* **1995**, *103*, 850.

(29) Munn, R. W.; Kelly, J. F.; Aicken, F. M. *Chem. Phys.* **1999**, *245*, 227.

(30) Munn, R. W. *J. Chem. Phys.* **2000**, *113*, 8774.

(31) Munn, R. W.; Malagoli, M.; Panhuis, M. I. H. *Synth. Met.* **2000**, *109*, 29.

(32) Tsiaousis, D.; Munn, R. W.; Smith, P. J.; Popelier, P. L. A. *Chem. Phys.* **2004**, *305*, 317.

(33) Spackman, M. A. *Chem. Rev.* **1992**, *92*, 1769.

(34) Coppens, P. *X-Ray Charge Densities and Chemical Bonding*; Oxford University Press: New York, 1997.

(35) Abramov, Y. A.; Volkov, A. V.; Coppens, P. *Chem. Phys. Lett.* **1999**, *311*, 81.

(36) Gopalan, R. S.; Kulkarni, G. U.; Ravi, M.; Rao, C. N. R. *New J. Chem.* **2001**, *25*, 1108.

(37) Hibbs, D. E.; Overgaard, J.; Piltz, R. O. *Org. Biomol. Chem.* **2003**, *1*, 1191.

(38) Munshi, P.; Spackman, M. A. Manuscript in preparation, 2006.

(39) Ferguson, G.; Glidewell, C.; Low, J. N.; Skakle, J. M. S.; Wardell, J. L. *Acta Crystallogr., Sect. C* **2001**, *57*, 315.

(40) *Bruker SMART, SAINT, ASTRO and XPREP− Data Collection and Processing Software for the SMART System*; Bruker Analytical X-ray Instruments Inc.; Madison, WI, 1995.
(41) Blessing, R. H. *J. Appl. Crystallogr.* **1997**, *30*, 421.
(42) Lenstra, A. T. H.; Van Loock, J. F. J.; Rousseau, B.; Maes, S. T. *Acta Crystallogr., Sect. A* **2001**, *57*, 629.
(43) Rousseau, B.; Maes, S. T.; Lenstra, A. T. H. *Acta Crystallogr., Sect. A* **2000**, *56*, 300.
(44) Whitten, A. E.; McKinnon, J. J.; Turner, P.; Pattison, P.; Weber, H. P.; Spackman, M. A., 2003. Data were collected at the Swiss-Norwegian beamline (BM1A) on a six-circle KUMA KM6-CH kappa diffractometer equipped with an Oxford Diffraction Onyx CCD detector. 3192 frames were collected with ω scans, with a detector-to-crystal distance of 36.0 cm. The wavelength was 0.71069 Å, and the temperature 100(2) K. The data proved unsatisfactory for charge density analysis, but served to provide a more reliable estimate of the structure factor for the (112) reflection.
(45) Tachibana, M.; Sato, S.; Kojima, K. *Acta Crystallogr.* **1996**, *A52*, C158.
(46) Stewart, R. F.; Spackman, M. A.; Flensburg, C. *VALRAY − User's Manual*, 2.1 ed. Carnegie Mellon University & University of Copenhagen, 2000.
(47) Cummins, P. G.; Dunmur, D. A.; Munn, R. W.; Newham, R. J. *Acta Crystallogr.* **1972**, *A32*, 847.
(48) Dovesi, R.; Saunders: V. R.; Roetti, C.; Causà, M.; Harrison, N.; Orlando, R.; Aprà, E. *CRYSTAL98 − Users Manual*, 1.0 ed.; Theoretical Chemistry Group of Torino, Italy, and CCLRC Daresbury Laboratory, England, 1998.
(49) Thakkar, A. J.; Koga, T.; Saito, M.; Hoffmeyer, R. E. *Int. J. Quantum Chem., Quantum Chem. Symp.* **1993**, *27*, 343.
(50) Spackman, M. A.; Byrom, P. G.; Alfredsson, M.; Hermansson, K. *Acta Crystallogr., Sect. A* **1999**, *55*, 30.
(51) Spackman, M. A.; Mitchell, A. S. *Phys. Chem. Chem. Phys.* **2001**, *3*, 1518.
(52) Gibbs, G. V.; Whitten, A. E.; Spackman, M. A.; Stimpfl, M.; Downs, R. T.; Carducci, M. D. *J. Phys. Chem. B* **2003**, *107*, 12996.
(53) Volkov, A.; Abramov, Y. A.; Coppens, P. *Acta Crystallogr., Sect. A* **2001**, *57*, 272.
(54) Whitten, A. E.; Dittrich, B.; Spackman, M. A.; Turner, P.; Brown, T. C. *J. Chem. Soc., Dalton Trans.* **2004**, 23.
(55) Spackman, M. A.; Jiang, B.; Groy, T. L.; He, H.; Whitten, A. E.; Spence, J. C. H. *Phys. Rev. Lett.* **2005**, *95*, 085502.
(56) Ellena, J.; Goeta, A. E.; Howard, J. A. K.; Punte, G. *J. Phys. Chem. A* **2001**, *105*, 8696.
(57) Stewart, R. F. Partitioning of Hartree−Fock Atomic Form Factors into "Core" and "Valence" Shells. In *Electron and Magnetization Densities in Molecules and Solids*; Becker, P., Ed.; Plenum: New York, 1980; p 427.
(58) Clementi, E.; Roetti, C. *At. Data Nucl. Data Tables* **1974**, *14*, 177.
(59) Stevens, E. D.; Coppens, P. *Acta Crystallogr., Sect. A* **1975**, *31*, 612.
(60) Kampermann, S. P.; Ruble, J. R.; Craven, B. M. *Acta Crystallogr.* **1994**, *B50*, 737.
(61) Pinkerton, A. A., Personal communication.
(62) Dittrich, B. Unpublished work, 2005.
(63) Kocher, N.; Henn, J.; Gostevskii, B.; Kost, D.; Kalikhman, I.; Engels, B.; Stalke, D. *J. Am. Chem. Soc.* **2004**, *126*, 5563.
(64) Leusser, D.; Henn, J.; Kocher, N.; Engels, B.; Stalke, D. *J. Am. Chem. Soc.* **2004**, *126*, 1781.
(65) Sorensen, H. O.; Stewart, R. F.; McIntyre, G. J.; Larsen, S. *Acta Crystallogr., Sect. A* **2003**, *59*, 540.
(66) Mallinson, P. R.; Koritsanszky, T.; Elkaim, E.; Li, N.; Coppens, P. *Acta Crystallogr.* **1988**, *A44*, 336.
(67) Becker, P. J.; Coppens, P. *Acta Crystallogr., Sect. A* **1974**, *30*, 129.
(68) Spackman, M. A. *J. Appl. Crystallogr.* **1987**, *20*, 256.
(69) Blessing, R. H. *Acta Crystallogr., Sect. B* **1995**, *51*, 816.
(70) Whitten, A. E.; Spackman, M. A. *Acta Crystallogr., Sect. B*. In press.
(71) Cole, J. C.; Cole, J. M.; Cross, G. H.; Farsari, M.; Howard, J. A. K.; Szablewski, M. *Acta Crystallogr., Sect. B* **1997**, *53*, 812.
(72) Cole, J. M.; Copley, R. C. B.; McIntyre, G. J.; Howard, J. A. K.; Szablewski, M.; Cross, G. H. *Phys. Rev. B* **2002**, *65*.
(73) *International Tables for Crystallography, Volume C: Mathematical, Physical and Chemical Tables*; Springer: New York, 2004.
(74) Ellena, J.; Goeta, A. E.; Howard, J. A. K.; Wilson, C. C.; Autino, J. C.; Punte, G. *Acta Crystallogr.* **1999**, *B55*, 209.
(75) McKinnon, J. J.; Mitchell, A. S.; Spackman, M. A. *Chem.—Eur. J.* **1998**, *4*, 2136.
(76) Spackman, M. A.; Byrom, P. G. *Chem. Phys. Lett.* **1997**, *267*, 215.
(77) McKinnon, J. J.; Spackman, M. A.; Mitchell, A. S. *Acta Crystallogr., Sect. B* **2004**, *60*, 627.
(78) Spackman, M. A.; McKinnon, J. J. *CrystEngComm* **2002**, *4*, 378.
(79) Spackman, M. A.; Byrom, P. G. *Acta Crystallogr., Sect. B* **1996**, *52*, 1023.
(80) Volkov, A.; Abramov, Y. A.; Coppens, P. *Acta Crystallogr.* **2001**, *A57*, 272.
(81) Bader, R. F. W. *Atoms in Molecules − A Quantum Theory*; Oxford University Press: Oxford, 1990.
(82) Bader, R. F. W.; Essén, H. *J. Chem. Phys.* **1984**, *80*, 1943.
(83) Birkedal, H.; Madsen, D.; Mathiesen, R. H.; Knudsen, K.; Weber, H. P.; Pattison, P.; Schwarzenbach, D. *Acta Crystallogr., Sect. A* **2004**, *60*, 371.
(84) Volkov, A.; Abramov, Y.; Coppens, P.; Gatti, C. *Acta Crystallogr., Sect. A* **2000**, *56*, 332.
(85) Volkov, A.; Coppens, P. *Acta Crystallogr., Sect. A* **2001**, *57*, 395.
(86) Volkov, A.; Li, X.; Koritsanszky, T.; Coppens, P. *J. Phys. Chem. A* **2004**, *108*, 4283.
(87) Bach, A.; Lentz, D.; Luger, P. *J. Phys. Chem. A* **2001**, *105*, 7405.
(88) Hibbs, D. E.; Overgaard, J.; Platts, J. A.; Waller, M. P.; Hursthouse, M. B. *J. Phys. Chem. B* **2004**, *108*, 3663.
(89) Hibbs, D. E.; Hanrahan, J. R.; Hursthouse, M. B.; Knight, D. W.; Overgaard, J.; Turner, P.; Piltz, R. O.; Waller, M. P. *Org. Biomol. Chem.* **2003**, *1*, 1034.
(90) Hibbs, D. E.; Austin-Woods, C. J.; Platts, J. A.; Overgaard, J.; Turner, P. *Chem.—Eur. J.* **2003**, *9*, 1075.
(91) Spackman, M. A. *Chem. Phys. Lett.* **1999**, *301*, 425.
(92) Matta, C. F.; Hernández-Trujillo, J.; Tang, T. H.; Bader, R. F. W. *Chem.—Eur. J.* **2003**, *9*, 1940.
(93) Whitten, A. E.; Radford, C. J.; McKinnon, J. J.; Spackman, M. A. *J. Chem. Phys.* **2006**, *124*, 074106.
(94) Bürgi, H. B.; Capelli, S. C.; Goeta, A. E.; Howard, J. A. K.; Spackman, M. A.; Yufit, D. S. *Chem.—Eur. J.* **2002**, *8*, 3512.
(95) Palmer, M. H.; Sherwood, P. *Z. Naturforsch.* **1996**, *51a*, 460.
(96) Stewart, R. F. *J. Chem. Phys.* **1972**, *57*, 1664.
(97) Brown, A. S.; Spackman, M. A. *Mol. Phys.* **1994**, *83*, 551.
(98) Aliev, A. E.; Harris, K. D. M. Probing Hydrogen Bonding in Solids Using Solid State NMR Spectroscopy. In *Structure and Bonding*; Springer-Verlag: Berlin, 2004; Vol. 108, p 1.
(99) Barnes, R. G.; Bloom, J. W. *J. Chem. Phys.* **1972**, *57*, 3082.
(100) Pyykkö, P.; Lähteenmäki, U. *Ann. Univ. Turku., Ser. A* **1966**, *93*, 2.
(101) Rowell, J. C.; Phillips, W. D.; Melby, L. R.; Panar, M. *J. Chem. Phys.* **1965**, *43*, 3442.
(102) Hunt, M. J.; Mackay, A. L. *J. Magn. Reson.* **1974**, *15*, 402.
(103) Destro, R.; Roversi, P.; Barzaghi, M.; Marsh, R. E. *J. Phys. Chem. A* **2000**, *104*, 1047.
(104) Roversi, P.; Destro, R. *Chem. Phys. Lett.* **2004**, *386*, 472.
(105) Stewart, R. F.; Davidson, E. R.; Simpson, W. T. *J. Chem. Phys.* **1965**, *42*, 3175.
(106) Koritsanszky, T.; Howard, S. T.; Macchi, P.; Gatti, C.; Farrugia, L. J.; Mallinson, P. R.; Volkov, A.; Su, Z.; Richter, T.; Hansen, N. K. *XD − A computer program package for multipole refinement and analysis of charge densities from diffraction data*, 4.10 ed.; Free University of Berlin, Germany, 2003.
(107) Smith, J. W.; Walshaw, S. M. *J. Chem. Soc.* **1957**, 4527.